BIOMIMETICS

A springtail-inspired multimodal walking-jumping microrobot

Francisco Ramirez Serrano, Nak-seung Patrick Hyun†, Emma Steinhardt‡, Pierre-Louis Lechère, Robert J. Wood*

Although legged robots have demonstrated effective mobility in some natural settings, as robot size decreases, obstacles in their environment become challenging to overcome. Small arthropods scale obstacles many times their size through jumps powered by mechanisms that overcome speed and power limitations of muscle alone. The motivation for this study was to explore the marriage of impulsive (jumping) and nonimpulsive (cyclic legged ambulation) behaviors in a centimeter-scale robot. Here, jumping is achieved by striking the ground with a bioinspired appendage connected to a parallel linkage. As the linkage configuration passes through the singularity, a torque reversal occurs whereby elastic energy slowly stored by force-dense velocity-limited shape memory alloy actuators is rapidly released. A passively driven elastic hinge is introduced in the striking arm to mediate ground contact forces and direct jumping. High-speed video recording of the 14-millisecond launch phase reveals previously undocumented takeoff dynamics closely resembling those of springtails. A dynamic model was derived, and an experimentally validated simulation was used to optimize the design of key components. The 2.2-gram, 6.1-centimeter-long mechanism achieved a maximum horizontal jumping distance of 1.4 meters (23 body lengths), surpassing that of similarly sized insects. The mechanism was integrated with an agile quadrupedal microrobot with leg articulation suitable to achieve the ideal jumping posture. The platform demonstrated repeatable directional takeoffs and upright landings, enabling complex maneuvers to overcome obstacles and gaps. Last, we used this bioinspired robot to offer reflection on hypotheses related to springtail jumping behavior.

INTRODUCTION

Microrobots, with a mass of less than 20 g and body length (BL) of less than 15 cm (*1*), have shown the capability to traverse natural terrain (*2*). However, unless climbing methods are used, legged devices cannot overcome obstacles larger than their body or leg lengths. Multimodal locomotion combining walking and jumping to cover a diverse set of environmental conditions is appealing for terrain robustness. Looking to biology for inspiration, researchers have used small arthropods to provide insights into miniature robot design because of their remarkable multimodal movement capabilities.

Mantis shrimp have one of the fastest accelerating predatory strikes (reaching 2.5×10^5 m/s^2 acceleration) in the animal kingdom (*3*). An overcentering torque-reversal mechanism powers these strikes (*4*). Springtails have a specialized appendage for jumping, a segmented jumping appendage called the furcula (or furca) that they unlatch onto the ground for rapid takeoffs [9.7×10^2 m/s^2 (*5*) and 115 BL (*6*)]. Trap-jaw ants are capable of extreme mandible movements, controlled by a friction latch, that serve for both prey capture and propulsion (*7*), accelerating their bodies to 8.6×10^3 m/s^2 and jumping over 20 BL. Other notable jumpers include fleas [3.2×10^3 m/s^2, 50 BL (*8*, *9*)], click beetles [3.7×10^3 m/s^2, 25 BL (*10*–*12*)], and plant lice [6.3×10^3 m/s^2 (*13*, *14*)].

The mechanisms that underlie each of these examples (and countless more) have been categorized as latch-mediated spring actuation (LaMSA) (*14*, *15*). LaMSA mechanisms are characterized by extreme temporal asymmetries between loading potential energy in a spring and the rapid release and conversion of potential energy to kinetic energy for jumps or strikes. Organisms that embody LaMSA principles tend to be small because of energetic constraints, such as favorable scaling laws affecting muscle-spring dynamics. Sutton *et al.* (*16*) determined that for animals, a crossover point exists at 2.5 g. Below this critical mass, spring-actuated devices jump higher than equivalently sized muscle-actuated jumpers. The evolutionary need for jumping locomotion at smaller scales is in part due to environmental asperity becoming large relative to the organism's body size [i.e., the size-grain hypothesis (*17*)].

Prior efforts on small-scale LaMSA jumping mechanisms have resulted in substantial progress on various fronts. Kurniawan *et al.* (*18*) developed a subgram jumper with an onboard energy source that could passively self-right and jump 5.75 BL, demonstrating power autonomy in a miniature LaMSA device. Koh *et al.* (*19*) developed two jumping platforms: a flea-inspired jumper requiring separate actuators for energy loading and jump triggering that could reach 1.2 m and a robot capable of jumping from a water surface (*20*). The latter is an example of the use of bioinspired robots to study behaviors that are unique to small animals (i.e., jumping from nonsolid matter). Ortega-Jimenez *et al.* (*21*) improved the aerial agility of a jumper using a torque-reversal catapult system through drag enhancers and mass modifications. Wang *et al.* (*22*) used a buckling cascade to trigger jumps with escape times on par with biological systems. This platform had sensors, a controller, and onboard batteries but could neither self-right nor steer the jump trajectory. Many of these example devices are composed of flexure-based mechanisms that enable them to emulate complex linkages at the scale of the insects that inspired their designs (*23*).

Walking-jumping multimodal robots require the ability to switch between modes, repeatable operation (i.e., the ability to reset, active or passive control of landing orientation, and jump-to-jump accuracy),

Harvard Microrobotics Laboratory, Harvard University, Cambridge, MA, USA.
†Present address: Elmore Family School of Electrical and Computer Engineering, Purdue University, West Lafayette, IN, USA.
‡Present address: Draper, Cambridge, MA, USA.
*Corresponding author. Email: rjwood@seas.harvard.edu

and reliable control (i.e., directional jumping, timing, and magnitude of energy release). These capabilities have been achieved in larger and heavier platforms, such as JumpRoACH (42.6 g, 11.5 cm long) (*24*), that leverage dc motors, but they remain a challenge at the microrobot scale, which uses other actuator types, such as dielectric elastomer actuators (*25*), piezoelectric actuators (*26*), or shape memory alloys (SMAs) (*27*). Zhakypov *et al.* (*28*) presented Tribot, a self-contained crawling-jumping platform (9.7 g, 5.8 cm long) that explored five distinct gaits, including jumping vertically and horizontally, somersaults to clear obstacles, walking on textured terrain, and crawling on flat surfaces. Another version of this robot included a compliant roll cage for self-righting. This robot used SMAs as both an actuator and spring to store potential energy, achieving jumps up to 5 BL. Many hybrid jumping-walking designs, such as Tribot and those at larger scales (*29*, *30*), lack the ability to change their orientation/heading while on the ground, limiting pretakeoff reorientation. A comparison of various jumping robots across key performance indicators is available in table S2.

Despite all of these breakthroughs in microrobotic jumping, more research is necessary to explore how individual mechanisms could direct jump trajectories to reach a specific target within a three-dimensional (3D) space reliably. A viable strategy is to integrate existing jumping mechanisms onto current walking microrobot platforms (*31*–*33*). In this case, careful considerations are needed to guarantee robust control and operation. Although some walking-jumping multimodal demonstrations exist in insect-scale robots, repeated jumping and landing have been mostly unexplored in legged, terrestrially agile microrobots capable of in-plane reorientation and dynamic maneuvers. Synergies between high-performance walking and jumping on a single platform may be key to unlock novel capabilities, in particular demonstrations of robots with the ability to position and orient the jumping mechanism for precise ballistic trajectories.

Here, a multimodal microrobot was developed by leveraging independent walk and jump mechanisms. The Harvard Ambulatory Microrobot (HAMR) (*34*), a quadrapedal walking robot, was used as the base walking platform. Its agile locomotion (*35*) and payload capabilities have already enabled the study of multimodal locomotion, such as walking on water (*1*) and on vertical surfaces (*36*). The core mechanism powering jumping is inspired by a torque-reversal linkage model found in the mantis shrimp striking appendage, where the impulsive striking is used to catch prey but not for the purpose of jumping (*4*). Previous work on the mantis shrimp mechanism demonstrates an extremely high acceleration without any impact/loading during the striking motion (*37*). We further built upon this impulsive behavior by designing a segmented passive jumping appendage not only to generate a high acceleration but also to provide an opportunity to mediate the impact with the ground during the impulsive motion. The segmented passive jumping appendage improves the aerial stability of the robot and the jumping performance (height and distance). This jumping mechanism uses a dynamic maneuver that had not been previously described that closely resembles springtail jump behavior.

We first describe methods to model, simulate, and optimize linkage parameters of the jumping mechanism. Our model describes the energy transfer from the hip spring to the ankle spring, which is then released onto the ground during the jump process. The simulation was validated first on an unoptimized prototype that can be seen in movie S2. A second prototype of the mechanism, able to achieve a peak jumping distance of 1.4 m (23 BL) (see movies S1 and S3), was created incorporating the results of the optimization to validate improved jumping trajectories. The mechanism demonstrates aerial stability, which enables upright landings. Figure 1 shows how the jumping mechanism was integrated within HAMR, an agile walking microrobot. Last, different terrain traversability scenarios using the jumping appendage are demonstrated, such as jumping on platforms, clearing gaps, jumping over obstacles, and repeated directional jumping. We also show potential for terrain interactions, such as jumping onto objects to push them, striking obstacles, and scooping up objects from the ground.

RESULTS

Impulsive system design overview

We used a mantis shrimp–inspired torque reversal catapult mechanism as a latch (which contained both geometric and contact latches) (*4*). This mechanism was capable of achieving a peak velocity of 41.2 m/s at the tip of the striking arm (*37*) and used a single actuator driving two degrees of freedom to both load and release energy (reducing weight and operational complexity compared with more independent degrees of freedom). The mechanism's striking arm had a large swing angle (180°), which induced undesired body torques when directly striking the ground (*21*) if the mass distribution, linkage lengths, and mechanism positioning were not carefully considered. Stored energy that was converted into body rotation was considered a source of inefficiency for the purpose of jumping. Furthermore, rotations made the landing orientation unpredictable. To improve jumping performance and robot orientation while airborne, we explored the effects of an added link (connected with a flexure-based hinge) on the striking arm. The two rigid links were renamed as the "tibia" and the "foot." Figure 2 (A and B) shows an

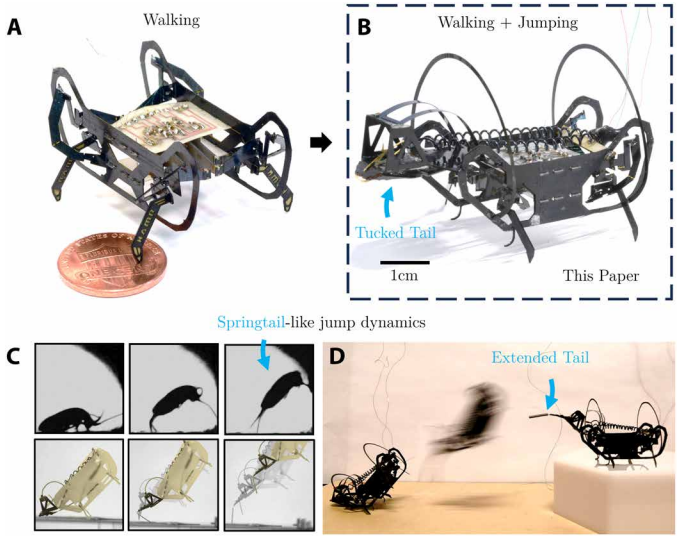

Fig. 1. A quadrupedal microrobot is enhanced with a torque-reversal catapult mechanism to achieve walking and repeated jumping. (**A**) The HAMR. (**B**) The 6.1-cm-long robot integrating HAMR with a 2.7-cm-long jumping mechanism mounted dorsally on the posterior. (**C**) Jumping frames highlight similar jump phases in our robot and springtails (*5*); both use a segmented jumping appendage to push off the ground. (**D**) The robot uses a dynamic maneuver to get into an initial upright position from which it jumps and lands onto an elevated platform.

CREDIT: SPRINGTAIL IMAGES COURTESY OF E. CHRISTIAN

overview of the robot components. Figure 3 (A and D) highlights the springtail anatomy that inspired this mechanism. Figure 4 presents the results of a dynamic jumping model based on a constrained Lagrangian formulation, and Fig. 5A includes a color-coded robot component breakdown and additional robot anatomy labels for parameters used in the optimization.

The LaMSA triggering mechanism was enabled by the kinematics of a five-bar linkage encompassing one variable-length link: the pulling tendon [implemented as an SMA actuator shown in red in Fig. 2 (A, B, and D)] and three rigid links connecting the tendon attachment point at the body a_b, the hip, the knee, and the tendon attachment point at the tibia a_k [shown in black in Fig. 2 (A and B)]. If the force vector at the knee attachment point a_k pulled below the a_k-knee segment, a counterclockwise torque was generated at the tibia (τ_{ti}), causing the tibia to remain in a tucked state, in contact with the femur as seen in Fig. 2 (A and C). The five-bar linkage shifted because of the tendon force while energy was loaded into the spring (shown in blue). A kinematically critical point was reached when the force vector aligned with the a_k-knee link. We referred to this point in the mechanism configuration space as the overcentering point. Pulling above the a_k-knee link (as illustrated) caused a clockwise torque τ_{ti}, the mechanism became unlatched, and the stored energy was released (Fig. 2, B and D).

The catapult mechanism consisted of six base elements. An FR-4 (flame-retardant type 4) glass-fiber composite chassis acted as a structural base. A spring steel buckling spring functioned as the main energy-storing element. A Nitinol SMA, which contracted when heated past its activation temperature (70°C), was attached to the jumping mechanism by means of a Kevlar string on one side and was slotted onto the back of the chassis as mechanical ground. The mechanism was assembled such that the tendon was always under tension to enable the latched and unlatched regimes previously described. Two conductive copper legs were connected to the SMA. The robot rested on a platform with conductive pads activated by a switch. A power supply of 6 V was connected to the conductive pads on the jumping platform. This powering method was advantageous because it enabled untethered jumping with repeatable initial conditions and decreased SMA degradation due to SMA overheating, because the current stopped flowing as soon as contact was lost during takeoff. In the resting position shown in Fig. 2C, the hind copper legs made contact with the pads, and the tip of the tibia rested on a tacky surface composed of X8 Gel-Pak.

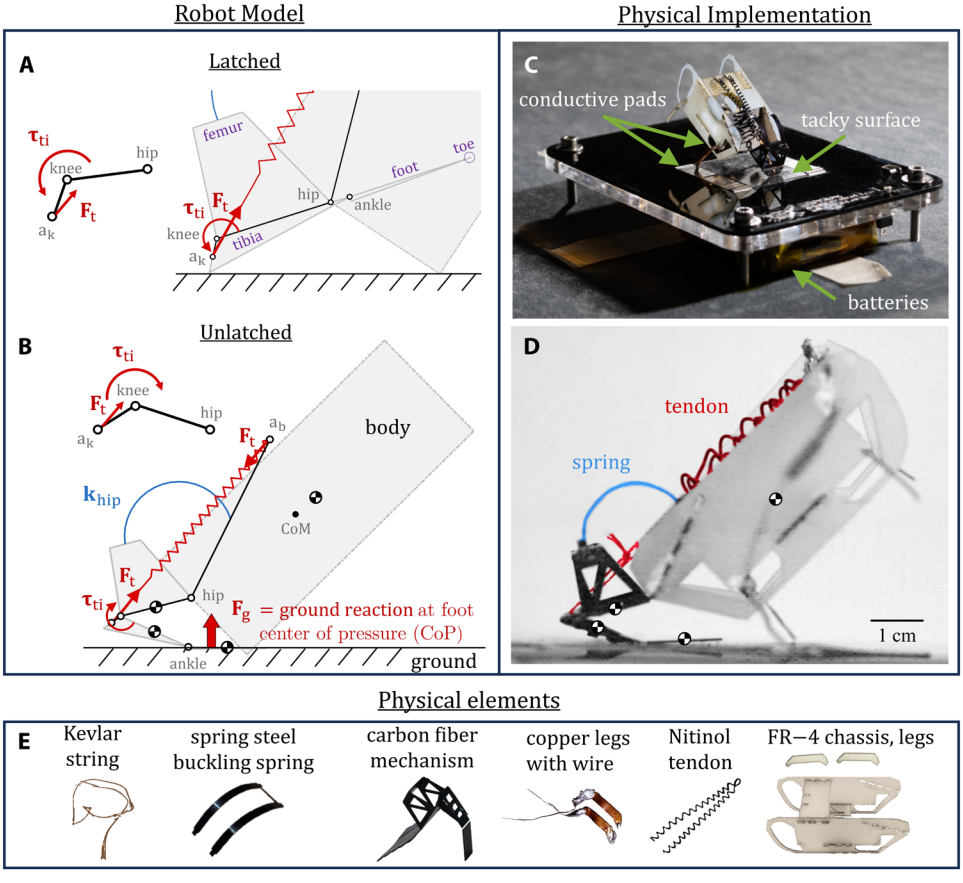

Fig. 2. Jumping mechanism model displaying latching mechanics and physical prototypes with a component breakdown. (**A**) The robot model in a latched state. As the tendon force, F_t, pulls under the knee joint, the ensuing torque on the tibia, τ_{ti}, causes it to remain in a tucked state against the femur. (**B**) As the linkages shift and the tendon force pulls above the knee joint, the torque at the tibia flips sign, triggering the jump. (**C**) The jumping mechanism sits on a battery-powered platform that heats up the SMA tendon, causing contraction. (**D**) A profile view of the jumping robot prototype depicted during part of the takeoff. (**E**) The base prototypes are composed of six elements.

Jump phases observed and biological importance

High-speed footage of the jumping prototype revealed six distinct phases. The phases of our jumping robot closely matched (qualitatively) the behavior observed in springtails striking the ground with their furculas to initiate a jump (Fig. 3B).

Springtails (Collembola) are hexapods usually less than 6 mm long. Springtail bodies could be globular or elongated. These creatures used a furcula, a segmented tail-like appendage that sat tucked underneath the body and released onto the ground to cause a jump (Fig. 3A). Both our mechanism's striking appendage and the springtail furcula had only two stable positions, flexed or extended.

The springtail jump sequence showed a transition from a latched state (frame I), where the jumping appendage was tucked, to an unlatched state (frame II onward). Frame I is the resting position with the jumping appendage tucked beneath the animal. Frame II is the manubrium angled downward after it had made contact with the ground; the dens was still coming down with the strike. Frame III shows when the dens made full contact with the ground and the hexapod pivoted at the dens-manubrium joint and pushed onto the ground, moving the body upward. Frame IV shows when the springtail was pivoting about the tip of the dens

(anatomically called the mucron). The position/inclination difference of the dens between frames III and IV suggested that some slipping occurred during the transition. Frame V is the furcula extended, straightening at the dens-manubrium joint. Frame VI captures the springtail losing contact with the ground. The latching mechanism from the robot presented in this paper was not inspired by springtails, whose release mechanism was not yet fully understood (*38*).

In the jumping robot, the jump phases were as follows. Phase I: During the energy loading phase, the SMA contracted, causing the five-bar linkage to shift while simultaneously loading energy onto the buckling spring. Bending at the hip joint caused the prototype chassis to recline/tilt backward, which can be seen in the real-time footage (movie S6). The loading phase ended at overcentering. A finer breakdown was possible, given that previous research on a similar overcentering mechanism unveiled an additional unlatched phase that took place when contact between the femur and the tibia was lost before overcentering. This was documented in (*4*), but we assumed that this additional phase did not substantially affect energy loading or the dynamics of unloading and included it as part of the energy-loading phase. Phase II: The torque at the tibia switched direction; the robot struck downward, and the tibia made contact with the ground and rolled onto the ankle joint. Phase III: From there, the robot pivoted about the ankle joint while the foot maintained contact with the ground. The pivot point then transitioned from the ankle to the tip of the foot (the "toe"). Phase IV: Some stick-slip behavior occurred where the toe detached from the surface, dragged on the surface, and stuck again. We highlighted in red the overall slipping distance. Phase V: Once the toe caught on the surface, the robot rotated about the toe until the toe slipped. Phase VI: The robot entered the aerial phase, following a ballistic trajectory until it landed. The grounded phases after overcentering, phases II to V, took 14.15 ms, 50 times faster than the aerial time of the robot and more than 500 times faster than the loading phase, highlighting the marked temporal asymmetries in this jump sequence. The jump captured corresponded to a horizontal distance, d, of 1.4 m; a robot mass, m, of 2.2 g; and a takeoff angle, α, of 56°, which we used to estimate (neglecting air resistance, using acceleration due to gravity $g = 9.8$ m/s^2) the takeoff velocity with the following equation (range of a projectile)

$$v = \sqrt{g \cdot d / \sin(2 \cdot \alpha)} \quad (1)$$

We calculated a takeoff velocity of ~20 m/s, at an average acceleration of 1.43×10^3 m/s^2, during the 14.15-ms jump phase.

Although latching dynamics (*39*) and jumping performance in springtails have been well studied (*5*, *6*), the jumping sequence of these animals is not entirely understood. In particular, the role played by the bending at the hinge between the dens and manubrium on the jumping performance has not yet been well described. A previous simulation of the jumping behavior of springtails by Brackenbury and Hunt (*40*) simplified the striking appendage into a single rigid link, but that study noted the presence of the junction between the dens and the manubrium and that the dens and manubrium effects might play a pivotal role in controlling jump performance. Therefore, we identified this joint as a critical design feature that was studied in more detail below.

Brackenbury and Hunt put forward several additional ideas about springtail jumping that our robot could help clarify. First, they suggested that adjusting the angle between the manubrial and dental components can alter the effective length of the furca, thereby influencing direction, height, spin, and range. They also proposed that the dens, unlike the manubrium, is relatively pliable and serves

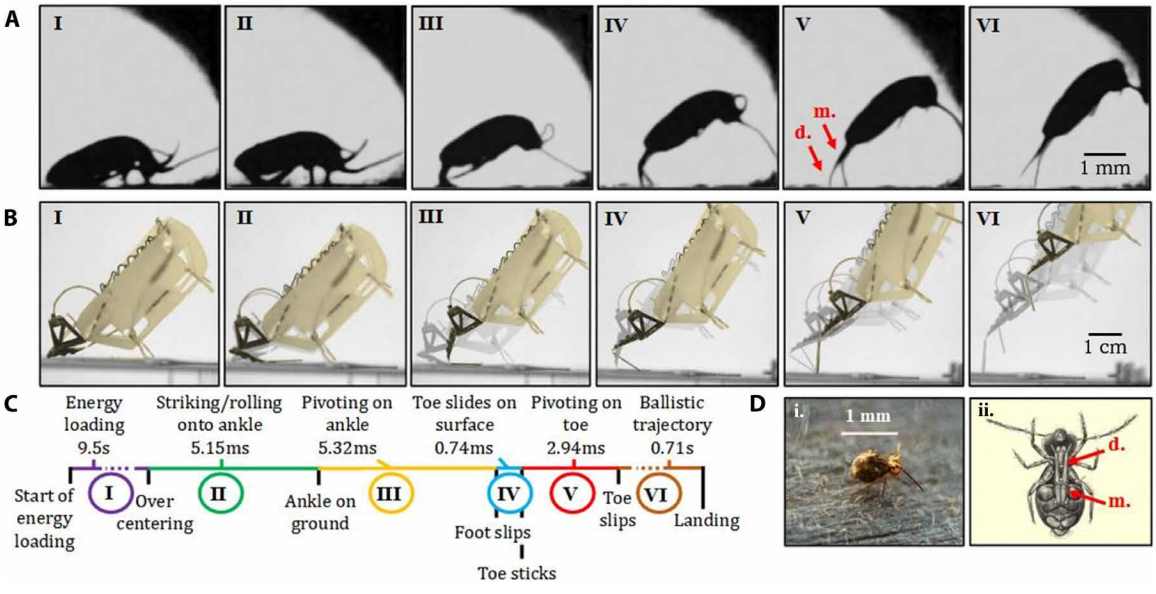

CREDIT: SPRINGTAIL IMAGES COURTESY OF E. CHRISTIAN (*5*); (D) FROM (*57*, *58*)

Fig. 3. Robot and springtail side-by-side jump sequences, broken down into six phases. (**A**) *Tomocerus vulgaris* jump sequence captured at 1450 frames per second (fps) courtesy of E. Christian (*5*). (**B**) Robot jump sequence as observed in movie S1. Video was recorded on a Phantom high-speed camera at 28,546.3 fps. For each jump phase, starting and ending frames are overlapped. (**C**) A chronological sequence of critical events with labeled transitions. The sequence highlights large temporal asymmetries between the loading phase I; the jumping phases II, III, IV, and V; and the aerial phase VI. (**D**) (i) A 1-mm-long globular springtail (tentatively identified as *Dicyrtomina ornata*) cropped from (*57*). (ii) Diagram of the ventral side of a springtail. The striking appendage called the furcula sits tucked underneath and is composed of a dens (d.) and a manubrium (m.) (*58*).

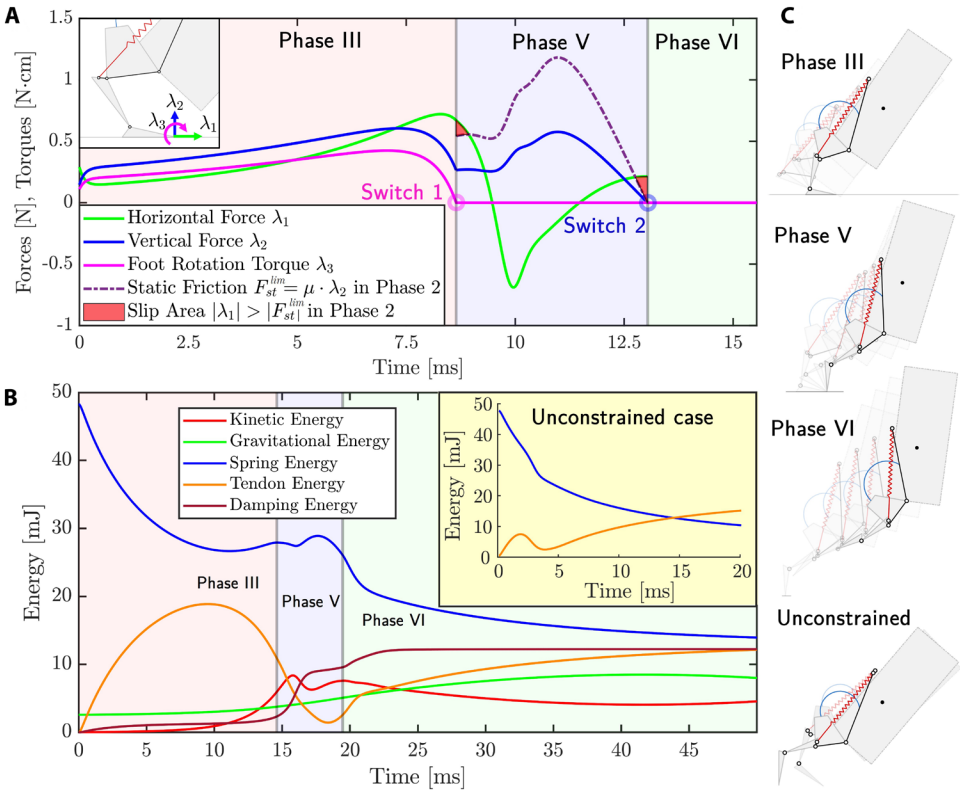

Fig. 4. A dynamic jumping model based on a constrained Lagrangian formulation predicts energies and forces during jumping. (**A**) Time evolution of the constraint forces at the tip of the foot. (**B**) Energy breakdown, with and without ground interactions; unconstrained case refers to the mode in which there is no contact with the ground. (**C**) Visualization of the different behaviors modeled.

primarily to prevent slippage rather than to extend the furca's lever arm. Last, they noted that most springtails likely tolerate a certain degree of spinning to maintain overall jumping efficiency.

Although our robot was approximately an order of magnitude larger than most springtails, it is important to note the substantial variation (30 times) in length scale among springtails. For example, species within the Needlidae family can be as small as 0.225 mm (*41*), whereas the Tomoceridae family, which also exhibits jumping behavior, ranges from 5 to 7 mm in length. Scale and morphology differences affected factors such as takeoff speed and angular velocities (*38*). However, the similarities in jumping mechanics, particularly the furcula placements and body orientation during takeoff, between our robot and larger springtails like Tomoceridae supported the relevance of our platform for investigating the proposed hypotheses. Thus, despite the size discrepancy, our robot remains a meaningful tool for exploring the dynamics of springtail jumping behavior. For this purpose, we first developed a dynamic model to describe the overall behavior of the jumping mechanism.

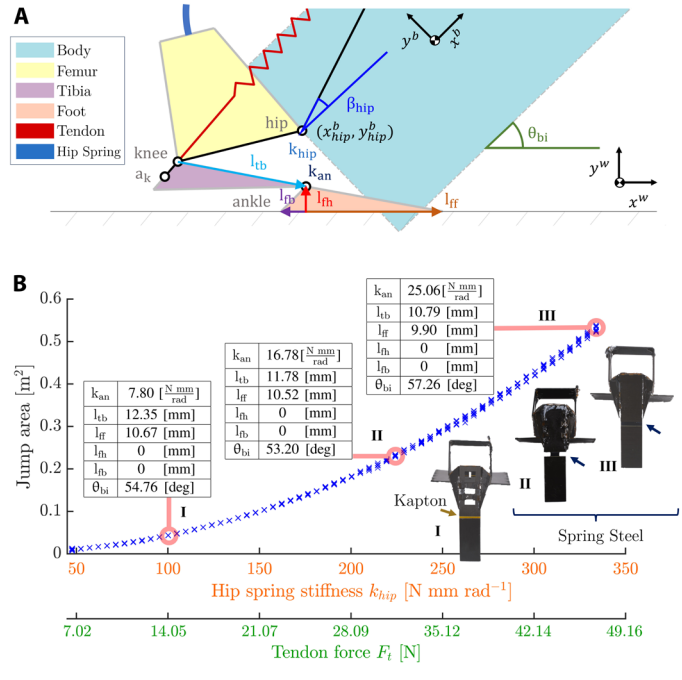

Fig. 5. Optimization-driven design evolution. (**A**) Optimization parameters and (**B**) design evolution as the hip spring energy increased and pulling tendon force increased. Each cross represents a particle that converged to an optimal solution after 500 iterations ($N \geq 6$ per spring stiffness/tendon force combination).

Dynamic modeling of jumping behavior

As observed in the multiple jumping phases captured in Fig. 3, the transition between phases occurred within a few milliseconds. Within those phases, the dynamics of the system markedly changed on the basis of the multiple contact constraints influenced by the ground reaction forces. The dynamics were similar to the heel-up and takeoff motion of bipedal walking robot dynamics, but the time evolution of our system was much shorter comparatively. We studied the sensitivity of design parameters (especially the parameters related to the additional segmented jumping appendage) within the dynamics via simulations and performed optimizations. The tendon was modeled as two constant equal and opposite forces, F_t, acting at the tendon attachment points a_k and a_b. The spring was modeled as a linear torsional spring acting at the hip. Given that the latching mechanism dynamics had been thoroughly studied, we focused our analysis on the new foot appendage. The system dynamics were described by a constrained Lagrangian mechanics model. For simplicity, we only modeled the dynamics after overcentering of the mechanism and once the ankle joint had come into contact with the ground (starting with Fig. 3A, phase II). We were interested in modeling the passive foot pivoting mechanics and understanding the ground reaction forces to predict the resulting jump trajectory. We used the body orientation $q_1 = \theta_{body}$; the hip $q_2 = \theta_{hip}$, knee $q_3 = \theta_{knee}$, and ankle $q_4 = \theta_{ankle}$ joint angles; and the body x-y positions ($q_5 = x_{body}$, $q_6 = y_{body}$) as generalized coordinates $\mathbf{q} \in \mathbb{R}^6$. The generalized coordinates can be seen on the diagram in fig. S1; additional details can also be found in the glossary. The ground reaction forces on the foot

contact surface could be combined into a single force acting at the center of pressure (CoP) (*42*), as represented in Fig. 2B. When this force left the foot support polygon, a rotation began. Goswami (*43*) extended this analysis to define the foot rotation indicator (FRI), which could be used to monitor foot rotation. For dynamic modeling simplification, we chose another approach: We modeled all ground contact forces by introducing three constraints acting at the tip of the foot (toe). In particular, we created a torque constraint to prevent the foot from rotating and penetrating the ground. The sign switching of this torque constraint was used to trigger foot rotation: The flat foot torque constraint acting on the foot about the toe was removed when the forces were such that the heel lifted away from the ground. Although modeling all forces at the toe captured the jump dynamics observed on the prototypes and in springtails, we lacked an explicit prediction of the ground reaction forces at the CoP during the flat foot phase (phase III).

The equations of motion derived from the Lagrangian are as follows:

$$M(\mathbf{q})\ddot{\mathbf{q}} + C(\mathbf{q},\dot{\mathbf{q}})\dot{\mathbf{q}} + G(\mathbf{q}) = \mathbf{F}_{\text{ext}}(\mathbf{q},\dot{\mathbf{q}}) \tag{2}$$

where $M \in R^{6\times6}$ is the mass matrix, $C \in R^{6\times6}$ is the Coriolis matrix, $G \in R^{6\times1}$ is the gravity vector, and $\mathbf{F}_{\text{ext}} \in R^{6\times1}$ are the generalized external forces. These forces are composed of a simplified linear torsional damping model used to characterize the damping at the flexure joints $\mathbf{F}_{\text{damp}} \in R^{6\times1}$, a constant tendon pulling force $\mathbf{F}_{\text{tendon}} \in R^{6\times1}$, and generalized holonomic constraint forces applied at the tip of the passive foot.

$$\begin{aligned}\mathbf{F}_{\text{ext}}(\mathbf{q},\dot{\mathbf{q}}) &= \mathbf{F}_{\text{damp}}(\dot{\mathbf{q}}) + \mathbf{F}_{\text{tendon}}(\mathbf{q}) + \mathbf{A}_{c1}(\mathbf{q})^T\lambda_1 \\ &+ \mathbf{A}_{c2}(\mathbf{q})^T\lambda_2 + \mathbf{A}_{c3}(\mathbf{q})^T\lambda_3\end{aligned} \tag{3}$$

$\mathbf{A}_{c1}(\mathbf{q})^T\lambda_1 \in R^{6\times1}$ prevents horizontal movement of the foot (slipping), $\mathbf{A}_{c2}(\mathbf{q})^T\lambda_2 \in R^{6\times1}$ prevents vertical movement (ground penetration), and $\mathbf{A}_{c3}(\mathbf{q})^T\lambda_3 \in R^{6\times1}$ prevents rotation of the passive foot into the ground (ground penetration). $A_{c123}(q) = \left[A_{c12}(q)^T\ A_{c3}(q)\right]^T = \left[A_{c1}(q)\ A_{c2}(q)\ A_{c3}(q)\right]^T$ represent the direction of the constraints in the generalized coordinates, and $\left[\lambda_1\ \lambda_2\ \lambda_3\right]^T = \lambda_{123}$ are the amplitudes of the constraints. $\tau_{123}(q,\dot{q}) = \left[\tau_{12}(q,\dot{q})^T\ \tau_3(q,\dot{q})\right]^T = \left[\tau_1(q,\dot{q})\ \tau_2(q,\dot{q})\ \tau_3(q,\dot{q})\right]^T$ are used to calculate the generalized constraint forces; see the Supplementary Materials for further details.

$$\lambda_{123} = \begin{cases} \left(A_{c123}(q)M(q)^{-1}A_{c123}(q)^T\right)^{-1}\tau_{123}(q,\dot{q}) & \text{if } \lambda_2 > 0 \wedge \lambda_3 > 0 \\ \left[\left(A_{c12}(q)M(q)^{-1}A_{c12}(q)^T\right)^{-1}\tau_{12}(q,\dot{q})\ \ 0\right] & \text{if } \lambda_2 > 0 \wedge \lambda_3 \le 0 \\ [0\ \ 0\ \ 0]^T & \text{if } \lambda_2 < 0 \end{cases} \tag{4}$$

By modulating the three constraints at the tip of the passive foot and under a no-slip assumption, we were able to model three phases: rotation and translation of the body as the tibia pivots about the ankle on the ground (corresponding to Fig. 3A, phase III), continued rotation about the tip of the passive foot (corresponding to Fig. 3A, phase V), and a ballistic trajectory of the system (corresponding to Fig. 3A, phase VI).

After the kinematics and dynamics were derived, we used a numerical solver to simulate jumps. Figure 4B displays the evolution of Lagrangian constraints at the tip of the foot. The switching between phase III and phase V takes place when the foot begins rotating away from the ground, which is detected by a zero crossing of the foot rotation torque constraint λ_3. Similarly, the second switching occurs after the zero crossing of the vertical force constraint λ_2. By measuring the static friction coefficient between the robot and the jumping pad, μ, to be 2.05, we were able to estimate the static friction limit force. Areas where the horizontal reaction force λ_1 exceeds the static friction limit imply a risk of slipping. We noticed that there were two regions prone to slipping at the beginning and end of phase V, as highlighted in Fig. 4A. The slip-risk zone that occurs during phase III could not be estimated because we did not know the forces at the CoP. Nonetheless, the modeled behavior matches the observed behavior and predicts the existence of the toe slipping phase (phase IV) in Fig. 3. Figure 4A shows that during the foot pivoting phase (phase V), the vertical forces increase, meaning that the toe actively pushes on the ground.

The robot consisted of four masses with (x, y) coordinates and angular velocities (ω) labeled $m_i, x_i, y_i, \omega_i \,|\, i \in [1,4]$ corresponding to the body, femur, tibia, and foot, respectively, which are shown in Fig. 2B. The total energy in the simulation at time t can thus be broken down into the following:

1) The kinetic energy due to the motion (translation and rotation) of the four robot body masses.

$$E^t_{\text{kin}} = \sum_{i=1}^{4}\frac{1}{2}m_i\left(\dot{x}_i^2 + \dot{y}_i^2\right) + \sum_{i=1}^{4}\frac{1}{2}m_i\cdot\omega_i^2 \tag{5}$$

2) The gravitational potential energy due to the four masses being subjected to Earth's gravity.

$$E^t_{\text{grav}} = \sum_{i=1}^{4} m_i\cdot g\cdot y_i \tag{6}$$

3) The spring potential energy stored and released in the hip, knee, and ankle because of the elastic deformation of the materials involved. The hip spring energy comes from the hip bucking spring (with a stiffness coefficient k_{hip}), and the knee and ankle joint spring potential energies come from the deformation of the flexure materials (with stiffness coefficients k_{kn} and k_{an}, respectively). All springs involved have corresponding rest angles labeled $q_{ir} \,|\, i \in [2,4]$.

$$E^t_{\text{spring}} = \sum_{i=2}^{4}\frac{1}{2}k_i\cdot\left(q_i - q_{ir}\right)^2 \tag{7}$$

The tendon force is nonconservative, meaning that the work done is path dependent. To determine the work at a specific time (t), we summed up all of the instantaneous works along the path taken. The tendon length at a specific time is noted as l^t_{tendon}.

$$E^t_{\text{tendon}} = \sum_{i=2}^{t} F_{\text{t}}\cdot\left(l^i_{\text{tendon}} - l^{i-1}_{\text{tendon}}\right) \tag{8}$$

We used a simplified linear torsional damping model to characterize the damping at the flexure joints at the hip, knee, and ankle, with corresponding damping coefficients b_2, b_3, and b_4. The damping force is also nonconservative, so we summed up all of the instantaneous works along the path taken.

$$E^t_{\text{damping}} = \sum_{i=1}^{t}\left(-\sum_{j=2}^{4} b_j\cdot\dot{q}_j^i\right) \tag{9}$$

The total energy in the isolated system described remains constant and is equal to the sum of all energies described above.

$$E^t_{\text{tot}} = \text{const} = E^t_{\text{kin}} + E^t_{\text{grav}} + E^t_{\text{spring}} + E^t_{\text{tendon}} + E^t_{\text{damping}} \quad (10)$$

In Fig. 2B, we can observe that energy released in the spring stretches the tendon, storing more energy (contraction releases energy). Any spring energy that is not released at the end of phase V when the toe leaves the ground is effectively lost for the task of jumping. We noticed an increase in spring energy on a grounded jump versus during an unconstrained jump when the striking appendage does not make contact with any surface. This indicates that energy is loaded onto the ankle joint and then released during the jump process.

Figure 3 shows the jumping sequence of the robot sample with the best jumping performance; however, the simulation was first validated on an unoptimized design. Movie S2 shows that initial prototype next to an animation of a simulated model trajectory. Although the simulation does not capture initial striking of the foot onto the ground nor the slipping in phase IV, the simulation correctly captures the overall timing and linkage positions during phases III, V, and VI.

Design optimization and resulting jump trajectories

We set up an optimization problem to explore parameter design of the foot, with particular focus on design parameters of the striking tail-like appendage as well as the positioning of the jump mechanism with respect to the robot body. Toward this goal, the following design parameters were introduced: the foot geometry, defined by a triangular shape of height l_{fh} and a base (the foot sole) composed of a heel length l_{fb} and a toe length l_{ff}; the ankle stiffness k_{an}; and the tibia length l_{tb}. Additional parameters included the jumping mechanism's hip positioning $x^{\text{b}}_{\text{hip}}$, $y^{\text{b}}_{\text{hip}}$, measured relative to the body center of mass (CoM) in a fixed body frame of reference (x^b, y^{b}), as well as the jumping mechanism base (the link between the hip and the body tendon attachment a_{b}) orientation β_{hip} with respect to the body x axis, x^{b}, in Fig. 5A. The initial angle between the body frame (x^{b}, y^{b}) and world frame (x^{w}, y^{w}) is noted as θ_{bi}. We opted to maximize the area beneath the CoM trajectory as our optimization objective. This objective reflects the biggest obstacle the robot could surmount and simultaneously optimizes both height and distance. To explore the evolution of the optimal design under varying energy releases, we increased the energy stored in the main hip spring k_{hip} as well as the pulling tendon force F_{t} and optimized the mechanism parameters according to the area criterion within reasonable bounds. We explored energy releases that correspond to jumping distances of up to 1.5 m.

The area A under a projectile taking off at velocity v and at an angle α with the horizon is

$$A = \frac{2v^4}{3g^2}\cos\alpha \sin^3\alpha \quad (11)$$

In a simple scenario, taking only the hip torsional spring energy into account and assuming all spring energy is converted into kinetic energy during takeoff, we have

$$E_{\text{kin}} = E_{\text{spring}} \quad (12a)$$

$$\frac{1}{2}k \cdot (\Delta q)^2 = \frac{1}{2}m_i \cdot v^2 \quad (12b)$$

$$v^2 = \frac{k \cdot (\Delta q)^2}{m_i} \quad (12c)$$

$$A(k) = \frac{2k^2 \cdot (\Delta q)^4}{3g^2 \cdot m_i^2}\cos\alpha \sin^3\alpha \quad (12d)$$

The optimization results shown in Fig. 5B highlight this proportionality: the area beneath the robot CoM $\propto k^2$. Over the range of spring energy/tendon force explored, the optimal linkage lengths did not vary widely. However, the model predicted that the ankle stiffness k_{an} must increase linearly with the hip spring stiffness k_{hip}. In addition, the foot height l_{fh} and heel length l_{fb} stayed null and were unaffected by the optimization; thus, we concluded that the extra foot weight brought by a toe height and heel extension did not present any advantages for jumping as modeled. The optimization results revealed an optimal takeoff angle across all hip spring stiffnesses of approximately 59°.

To vary ankle stiffness, different hinge materials (Kapton and spring steel) and flexure dimensions were used. High-speed footage revealed three scenarios for a given hip spring energy release: The ankle stiffness was too high, the ankle stiffness was too low, or the ankle stiffness was around the optimal value. If the ankle stiffness of a jumper was too low for a given hip spring energy, slipping of the foot occurred during phase III, and the toe did not catch on the surface. In this case, there was no toe-pivoting phase (phase V) (movie S5). If the ankle stiffness was too high for the given hip spring energy, there was no pivoting on the ankle joint (phase III). High aerial stability with little to no body rotation was achieved by the mechanism in all three scenarios; see movie S4.

Two additional prototypes were built, one with motion capture markers (prototype shown in fig. S2 and corresponding trajectory shown in red in Fig. 6A), and one with two parallel SMAs to maximize pulling strength and enable higher spring stiffness (prototype shown in fig. S3, corresponding trajectory shown in Fig. 6B). The motion capture–tracked jumping prototype was equipped with a weaker buckling spring (7-mil-thick spring steel versus 15-mil-thick spring steel) because of the limited tracking volume of the Vicon motion capture system. Both experimental trajectories matched the corresponding simulated trajectories with equivalent hip spring stiffnesses shown in Fig. 6: $k_{\text{hip}} = 157$ N·mm·rad^{-1} matched the motion capture measured trajectory, and $k_{\text{hip}} = 334$ N·mm·rad^{-1} matched the double SMA filmed trajectory. Both measured jumps undershot the target optimal takeoff angle of 59° (52° for the motion capture experimental trajectory and 56° for the double SMA trajectory). This occurred because the initial conditions from the simulation differ from those in the real experiments; the simulation started after the mechanism was unlatched; however, during the experiments, the robot must first load energy. During the loading phase, the body angle varied, making it difficult to predict the initial resting robot angle to achieve a target takeoff angle. We highlight that constructing these devices is difficult. When pushed to their mechanical limits, the device may fail after a single jump if the ankle is permanently deformed, changing its stiffness, or if the SMA loses its pulling ability because of overheating if the spring used is too stiff. For these reasons, we relied on our models to predict performance and guide designs and then prototyped only the most promising candidates.

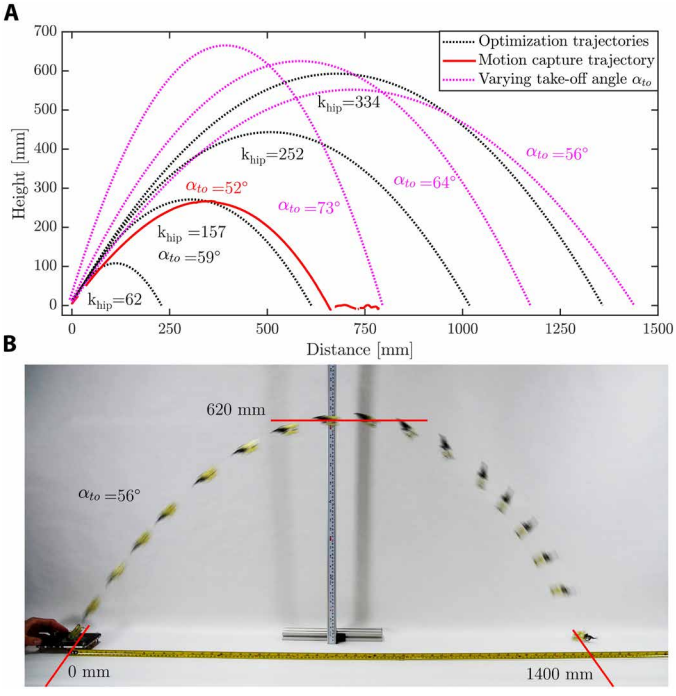

Fig. 6. Jumping trajectories. (**A**) Predicted optimal trajectories for various hip spring energy values are depicted in black (for a takeoff angle of 59°). The red trajectory represents a measured prototype jump trajectory in a motion capture setup. The magenta trajectories correspond to different takeoff angles (56°, 64°, and 73°) from the optimization solution for k_{hip} = 334 N·mm·rad^{-1}. (**B**) Frames from the peak 1.4-m jumping distance achieved by the mechanism are overlapped to showcase the trajectory.

The robot takeoff angle was altered by changing the robot's initial body angle in the simulation. In Fig. 6A, additional trajectories are traced in magenta. In the physical implementation, the robot rested on its hind legs, which can be angled forward or backward, altering the resulting takeoff angle. Together, these results showed a promising avenue for jump trajectory modulation and landing target selection. Although the simulation was capable of producing designs that do not rotate in the air and are highly stable, when optimized for jumping distance, the best optimization solutions always included aerial rotations. We therefore reached the same conclusion as with the biologically inspired springtail jumping model developed by Brackenbury and Hunt (*40*) that it is possible to reduce or even eliminate spinning, although this comes at the cost of efficiency. We hypothesized that deviations between simulations and experiments are primarily due to three factors: First, the simulation modelled the robot's mass as four distinct point masses, neglecting their individual moments of inertia. Second, the simulation assumed perfect hinges and constant distances between them, ignoring potential manufacturing imperfections and delamination between structural, adhesive, and compliant layers near the joints. Last, external forces (e.g., air friction) could affect the robot dynamics but were ignored in the equations of motion.

Integration within a quadrupedal microrobot

The jumping mechanism was integrated within the HAMR platform (*34*) as shown in Fig. 7. This platform uses piezoelectric actuators (part M) to drive individual lift and swing degrees of freedom on each leg (part J) through a spherical five-bar transmission (part Q). This robot is capable of a high-speed walking performance (8.5 BL/s) (*44*), achieving numerous different gaits (walk, trot, pace, jump, bound, pronk, and crab) (*45*), payload-carrying capabilities [the HAMR platform can carry up to two times its body weight (*46*)], and resistance to drops from heights (capable of >10-cm drops without damage). We used a tether for power and control (part D) for experimental convenience, although an autonomous version of the walking robot with onboard power exists (*47*). The peak payload for the HAMR platform used is 2.9 g; therefore, it should be able to sustain the combined payloads from the jumping mechanism (1.26 g) and from the battery and controls (1.36 g). We anticipated that the PowerStream's GM300910 battery would be sufficient to power both walking and jumping given the properties of the actuators used in this paper.

The jumping mechanism was assembled on the back of the robot, and a dynamic maneuver with the bound gait was used to transition into the upright position needed to initiate a jump, similarly to the initial position of the previously described prototypes. Multiple adaptations were needed to integrate the jumping mechanism on the device.

Foot sole surface

In the robot implementation, the tibia (part N) and foot (part P) surfaces that come in contact with the ground during jumping were covered with the same X8 Gel-Pak material that was previously used on the jumping platform (seen in Fig. 2C) to increase friction and prevent slipping (part L). The X8 Gel-Pak surface, engineered for high shear resistance with minimal normal adhesion, enhanced friction between the contact surface and the jumping appendage tip, ensuring negligible adhesion forces during detachment.

Takeoff position hind leg support

Hooks (part G) were attached to the chassis because HAMR's rear legs (part J) were too compliant to support the weight of the robot in the upright takeoff position.

Jumping mechanism mounting

The jumping mechanism base (part S) was shifted toward the back of the robot so that the striking appendage (tibia and foot) would not make contact with the piezoelectric actuators (part M) beneath the robot when retracted. This served a dual purpose because shifting the center of weight backward helped the robot in its dynamic transition from a horizontal walking position to an upright takeoff position.

Reloading tendon

A retracting tendon (part R) made from a sheet of silicone rubber was assembled to reload the striking arm and enable repeated jumping. On one end, it was threaded through a rectangular hole in the femur, to facilitate tendon tensioning during assembly, and glued. On the other end, it was glued to a Kevlar string near the knee joint so that the tendon could maintain its orientation in all striking appendage configurations. This tendon was antagonistic to the striking motion and was designed to provide the minimum necessary tension to reset the striking appendage to minimize the effects on jumping performance.

Roll cage

Two landing orientation rings (part C) were slotted and glued on the top side of the platform to aid the robot in rolling/bouncing (after landing) to the correct orientation, enabling it to jump again. These rings may also protect more sensitive parts such as the top-facing circuit board (part H).

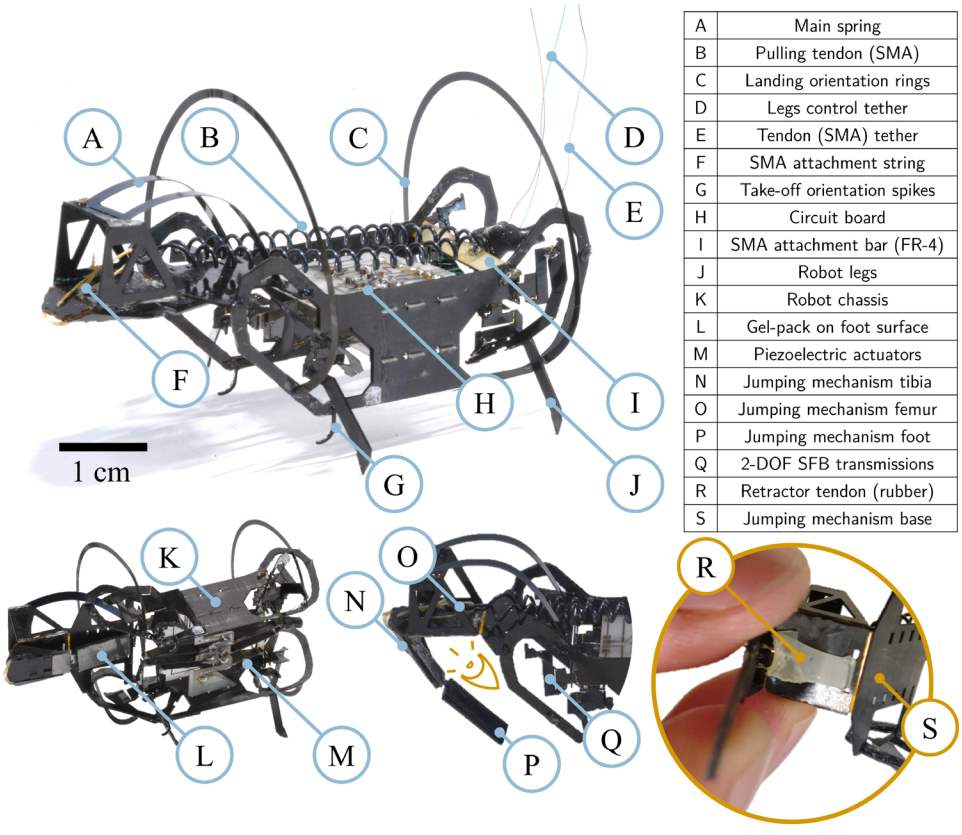

A	Main spring
B	Pulling tendon (SMA)
C	Landing orientation rings
D	Legs control tether
E	Tendon (SMA) tether
F	SMA attachment string
G	Take-off orientation spikes
H	Circuit board
I	SMA attachment bar (FR-4)
J	Robot legs
K	Robot chassis
L	Gel-pack on foot surface
M	Piezoelectric actuators
N	Jumping mechanism tibia
O	Jumping mechanism femur
P	Jumping mechanism foot
Q	2-DOF SFB transmissions
R	Retractor tendon (rubber)
S	Jumping mechanism base

Fig. 7. The HAMR integrated with the LaMSA jumping module developed in this paper.

SMA attachment

A 508-μm-thick FR-4 rectangular beam (part I) that hooks onto the chassis at the back of the robot was used as an attachment point for the SMA. Carbon fiber is conductive, which is why FR-4 was used instead to prevent a short circuit. The SMA was tethered by a copper wire to the power source. The robot chassis (part K) was reinforced to prevent the robot from buckling because of the SMA contraction. SMAs (part B) manufactured for this robot had resistances of around 0.6 ohm and could be contracted through joule heating in 30 s or less, depending on the contraction current used (0.48 A corresponds to 9.5 s). Wires [26 American Wire Gauge (AWG)] were soldered onto the SMA (part E) (shrink tubing was used for additional connection support).

The robot jumping mechanism was equipped with a thinner buckling spring to limit jumping distance (compared with the buckling spring used to achieve the 1.4-m jump shown in Fig. 3). This was done to prolong the life span of the robot because further quantification of fall-related damage resistance in different landing orientations is the subject of a future investigation. A single SMA configuration was used to reduce weight, which affects robot walking. The robot is 3.1 cm tall, 3.7 cm wide, and 6.1 cm long and weighs 2.7 g versus the 2.2-g double SMA configuration prototype.

Robot operation and demonstrations

The robot's piezoelectric actuators were controlled from a high-voltage amplifier at 210 V to send gait commands consisting of lift and swing signals with different frequencies, phases, and amplitudes (*48*). A separate power supply was used to trigger the jumping mechanism. The robot first walked to the desired takeoff position using a trot gait (20-Hz frequency) and then adjusted its direction with an oriented crabbing left/right gait. From here, a bounding gait at 4.5 Hz allowed the robot to oscillate near the body resonant frequency. The robot pivoted on the hind hooks, eventually reaching a tipping point when the robot fell backward onto the tibia (part N). This could take anywhere between 1 and 10 s and was affected by the slope the robot was on (if the robot faced an incline, the maneuver was easier to perform) and the positions of the tethers, which affected the robot mass distribution. A power source was activated and drove sufficient current (6 V, 0.2 to 0.5 A) through the SMA to cause contraction and triggering of the jump (20 to 30 s). After landing, the retracting tendon pulled the tibia over the overcentering point, causing a torque reversal that kept it in a tucked state against the femur, effectively resetting the mechanism. This process was slow (45 s) because the SMA, when still hot, pulled directly against the retracting tendon at this stage, and additional time was necessary for the SMA to cool to transition back to its original state. Figure 8A shows the different motion primitives that can be pieced together into more complex behaviors.

Various multimodal locomotion scenarios were explored. In Fig. 8B, the robot can be seen jumping onto a raised platform that is 3.5 cm tall and 9.6 cm in the longest planar dimension and has a relatively small landing area (60 cm^2) compared with the robot (robot transverse plane area is 23 cm^2). This demonstration highlighted the landing stability, aided by the compliance of the robot legs, as well as the achievable jump accuracy for landing on a small target. In Fig. 8C, the robot can be seen clearing a gap and landing onto a 10° incline. In this demonstration, the robot landed on its extended striking appendage and hind hooks. However, as the tendon retracts, the striking appendage exerts a moment on the ground and rotates the robot body back into a horizontal orientation from which it can walk, highlighting another mechanism for landing robustness. Figure 8D shows the robot jumping from an 8° inclined surface onto a 9° decline surface and over a banana. Upon landing, the limited tether length caused the robot to rotate.

Aside from these terrain traversability demonstrations, the robot was recorded interacting with its surrounding environment in unique ways using the jumping appendage. Microrobots limited to a 2D surface have previously demonstrated the ability to push objects around (*49*). However, because of the low mass of an individual robot, multiple robots were necessary to push objects with greater masses. The addition of the jumping mechanism enabled the robot to exert greater instantaneous forces on objects in its environment than using the legs and body alone. For example, in Fig. 8E, the robot

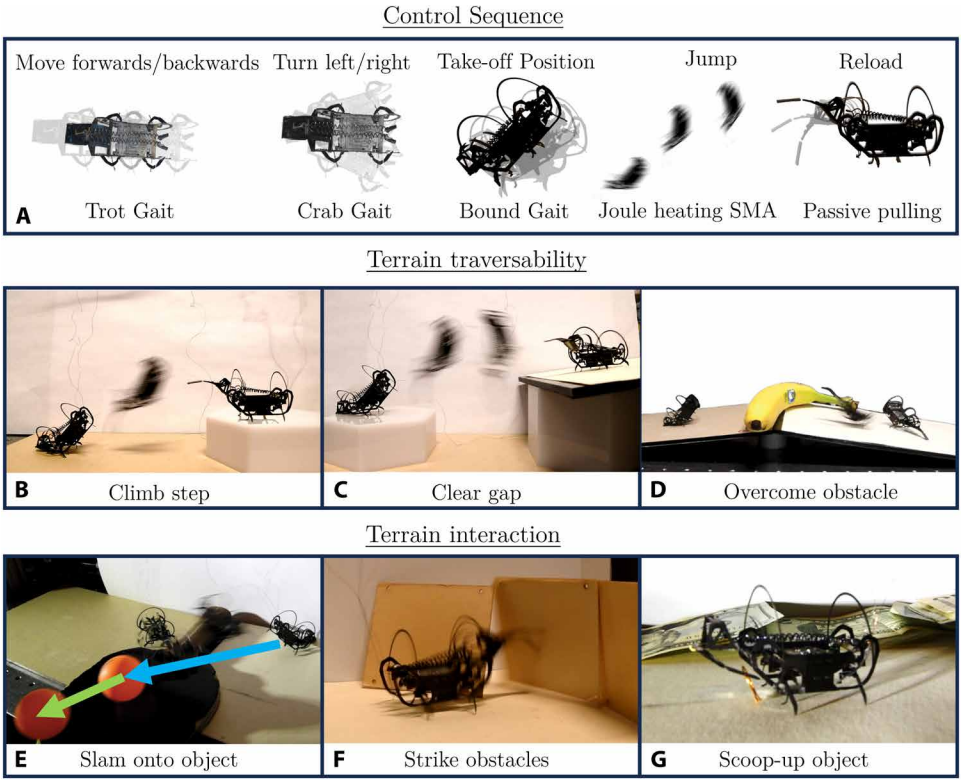

Fig. 8. Robot multimodal movement capabilities and various terrain interactions. (**A**) Multimodal movement was achieved by chaining together different motion primitives. Examples include trot (forward/backward), crab (left, right, and with an additional turning component), and bounding gaits. In addition, the jump was controlled by passing a constant current through the SMA. Reloading occurs passively as the SMA cools and the extended tendon recoils. (**B** to **D**) Terrain navigation demonstrations where the robot jumps onto a raised platform, clears a gap onto an inclined terrain, and overcomes an obstacle, respectively. (**E** to **G**) Additional terrain interactions made possible by the jumping mechanism include jumping onto objects to move them, striking when the robot is upright to hit walls, and scooping up objects with the retracting tail, respectively.

jumped onto a standard ping-pong ball, causing a transfer of momentum that pushed the ball off the racket. The ping-pong ball weighs 2.7 g, more than the robot itself. In Fig. 8F, the robot struck with the appendage while in a horizontal position with all legs touching the ground, which collapsed a thin wall obstacle. Last, in Fig. 8G, the robot was positioned so that the reloading motion of the mechanism allowed the foot to pick up a wire ring in a scooping motion. The ring sat on the foot hinge, and the robot could walk around with this payload. Additional demonstrations included rolling on the cage upon landing, two consecutive jumps (repeated jumping), jumping on leveled flat terrain, and jumping from natural terrain (see the Supplementary Materials for videos of each of these behaviors).

DISCUSSION

Here, a torque reversal catapult LaMSA mechanism with a segmented striking arm was introduced. High-speed footage revealed six distinct temporal phases where the robot pushed off the ground with the tip of the tibia and, subsequently, the tip of the foot. This dynamic maneuver leads to highly stable aerial trajectories with minimal body rotation. The jump behavior was simulated through a constrained Lagrangian formulation, and the mechanism was optimized for jumping height and distance by increasing the area under the trajectory of the CoM, a proxy for jump performance. The optimization results reveal the need to calibrate the stiffness of the hinge at the striking appendage (the ankle) as a function of the energy released by the LamSA mechanism. The simulation predicted the occurrence of slipping observed in the high-speed footage of jumping prototypes. Mechanisms with various ankle joint stiffnesses were assembled, and the recorded jump trajectories closely matched those predicted by the model, validating the simulation. The 6.1-cm-long, 2.2-g jumping mechanism achieved a peak jumping distance of 140 cm (23 BL) (see movies S1 and S2). This surpasses the jumping performance of similarly sized insects: For instance, an 8-mm-wide, 50-mm-long male locust weighing 1.5 to 2 g can jump 0.8 to 0.95 m (19 BL) (*50*). The mechanism's jumping capability is also on par with robots of similar size and weight, including the Flea Robot (3 cm, 2.5 g) that jumps 120 cm (40 BL) (*19*) and the EPFL Jumper (5 cm, 7 g) that reaches 138 cm (28 BL) (*51*).

The jumping dynamics of our robot closely resembles the jump sequence of springtails, small hexapods (1 to 10 mm long) that jump using a segmented tail-like appendage called the furcula. This jumping appendage consists of a manubrium and dens, which are functionally similar to the tibia and foot in our robot. Insights from the experimental results and simulations provide evidence to address the springtail structure-function hypothesis laid out by Brackenbury and Hunt (*40*) in 1993: The ability to vary the effective length of the furca by altering the angle between the manubrial and dental components would provide the means to control not only direction but also height, spin, and range (*40*). On the basis of past literature, it seems that springtails do not use jumping for typical locomotion but instead as an escape mechanism (*52*). Control of body attitude may be of secondary importance to simply escaping predation, whereas robots with similar mechanisms would benefit from more jump control. A future improvement for height, spin, and range control is to orient and position the robot body and jumping mechanism before takeoff.

Our robot simulation and physical implementation did not allow the robot to control the angle that corresponds to the springtail manubrium and dens joint during jumping and used a spring instead to passively drive this angle. Changes in the stored energy at the ankle joint equate to different effective furca length changes, which results in various jumping behaviors. It takes 4.8 ms for the jumping maneuver of 2-mm-long springtails (*38*) and 14.2 ms for our 6-cm-long robot. Independent control of the striking appendage hinge angle during takeoff on a robot of this size, and with appropriate bandwidth to match the speed of the striking appendage, would now

pose a substantial engineering challenge. Here, we focused instead on mechanism design and positioning for trajectory control. In jumping microrobots, jumping trajectory control is a more common objective than takeoff time duration (i.e., a preference for control over rapid escape). The striking appendage in springtails is tucked beneath and closer to the center of the hexapod than in our robot, where the striking appendage is positioned further back with regards to the body CoM. Our mechanism also requires an upright maneuver first before jumping so that the mechanism is in contact with the ground, whereas with springtails, the mechanism is always close to the ground. Centered mechanisms will provide a better mass distribution for the purpose of walking, and a mechanism that is always close to the ground will enable a faster jump. Although the springtail jumping configuration and operation may not allow for much trajectory control, by placing the mechanism at the back and angling the robot body before jumping, our simulation predicts the ability to achieve multiple heights, spin rates, and horizontal jump ranges. This can be achieved by varying initial jump conditions such as the body angle. Altering foot geometry, such as toe height or ankle position, also alters the effective length of the furca and is another promising approach for trajectory control.

A second insight from past springtail literature involves the function of the distal portion of the jumping appendage: The dens, unlike the manubrium, is a quite flaccid structure, and its role during leaping may be more concerned with providing friction, i.e., preventing slippage, than adding to the lever arm effect of the furca (*40*). The robot component equivalent to the dens, namely, the foot, plays a similar role in using friction to prevent slipping. On our jumping robot prototypes, both flaccid and overly stiff ankle configurations led to premature slipping; i.e., slipping began before the hip spring released all of the stored potential energy. The simulation also shows that during the toe-pivoting phase (phase V, Fig. 4A), the robot foot (dens) pushes against the ground, increasing friction forces. There are a multitude of other factors that affect slipping, including the materials that are in contact, the geometry of the surfaces, and the normal forces pressing down on the ground. Movie S5 includes videos of the robot slipping under various conditions.

Last, Brackenbury and Hunt (*40*) also note that most springtails presumably tolerate a degree of spinning in the interest of preserving efficiency. Our simulation results suggest that this hypothesis is correct because the optimal designs include body rotations, although the design space allows for designs that induce minimal body moments during takeoff (see movie S4). However, the optimal solutions do induce body rotations, suggesting that spin is a byproduct of increased jumping distance in springtail dynamics.

A tradeoff exists between optimizing for jump distance and minimizing aerial rotations to promote successful landings. If rotations substantially affect landing success, then they should be the main objective of optimization and control schemes. In our multimodal walking-jumping robot, upright landings are achieved by having reduced aerial rotations, which increase the probability of the robot landing upright. For high-energy jumps where the robot bounces off the ground regardless of the landing orientation, optimizing for distance becomes more relevant. In this case, the focus should be shifted to landing strategies, like aerial reorientation or self-righting mechanisms. This aligns with the approach seen in springtails (*53*). A general strategy may involve maximizing takeoff velocity and minimizing posttakeoff angular momentum when possible. The ability to modulate these two objectives is a key feature of our jumping mechanism design. To demonstrate the ability to overcome obstacles, we integrated the mechanism onto a quadrupedal robot and achieved repeated directional jumping and landing. The platform used in the demonstrations in Fig. 8 was limited in jumping distance (compared with the jumping prototype shown in Fig. 6) for multiple reasons. First, we used a weaker spring and SMA combination to reduce weight because additional mass hinders walking performance. Second, further experiments are needed to guarantee the quadrupedal robot's robustness upon falling from large distances at an arbitrary orientation. Third, stronger pulling forces than those used on the current platform cause the robot chassis to buckle onto itself. Last, the retracting tendon is an antagonist to the jumping mechanism and hinders performance.

The platform was able to climb steps, clear gaps, overcome obstacles, passively roll to orient itself, jump repeatedly, and orient itself on the ground before jumping (Fig. 8A-D). In addition, the mechanism opens the door to novel terrain interactions, including slamming onto objects to move them, striking obstacles to knock them over, and manipulating objects with the retracting tail-like appendage (Fig. 8, E and F).

There are numerous future research directions stemming from this work, with many related to alternative design choices. First, motivated by the limited payload of robots at this physical scale, using a structural chassis element as the jumping mechanism's energy storage element (*54*) could reduce the overall mass and better distribute mass to improve walking performance. In this scenario, the buckling of the robot chassis under SMA loading could be used as the primary energy source, eliminating the need for a separate spring. Now, the robot jump maneuver begins with a dynamic tilting motion to reach a fixed stable desired inclination before jumping by resting on posterior hooks. In future designs, a jump could be triggered to release at a specific orientation of the dynamic tilting motion. Although it is challenging to modulate the striking force, as shown in Fig. 6, taking off with different body angles enables different parabolic jump trajectories. The mechanism explored here can easily be adapted to strike the ground or push off by adapting the distance of the mechanism to the ground, making it suitable to explore various modes when jumping from different media (*55*). Furthermore, future work will focus on a thorough characterization of the reloading tendon to better understand its impact on overall jumping performance. In addition, exploring self-orientation using mechanism momentum, as demonstrated in movie S9, will be crucial for developing weight-efficient self-righting strategies. Additional considerations regarding mass distribution will be necessary to maintain jumping and walking functionality on a power-autonomous version of our robot. For example, the bounding gait used by the walking-jumping platform to get into a takeoff position requires the CoM of the robot to be near the hind legs (pivot point); however, the hind legs of the robot were unable to fully lift off the ground with the additional weight as seen in movie S6. A possible solution will be to position the jumping mechanism directly under the robot to better distribute the mass; this configuration was used in movie S9.

MATERIALS AND METHODS

Fabrication of the torque reversal catapult mechanism and jumping robot prototypes

The torque reversal catapult mechanisms were developed by first using the rapid prototyping workflow for microelectromechanical systems (pop-up MEMS) devices (*56*) before using the legacy pop-up

MEMS process to create more robust samples (*23*). The fabrication technique is described in (*4*) and consists of micromachining with an Oxford E series ultraviolet laser the five structural layers: two carbon fiber composite layers, two Pyralux acrylic adhesive layers, and a Kapton film. These layers were then stacked and laminated in a heated press. The resulting laminate structure underwent a final laser cutting step to release the target structure. The mechanism was popped out and locked with cyanoacrylate glue (Loctite 411). Single-layer structural elements made out of carbon fiber composite (Fig. 7, parts C and G), FR-4 (10-mil FR-4 for the prototype jumping mechanism chassis and legs shown in Fig. 2E and 20-mil FR-4 for Fig. 7, part I), blue tempered spring steel (all buckling springs as in Fig. 7, part A), or copper (Fig. 2E, hind legs) were also machined with the Oxford E series laser.

Buckling springs were made using 5- to 15-mil-thick blue tempered spring steel 1095 purchased from McMaster-Carr. After machining, springs were bent manually to provide minimal tension during the neutral phase of the mechanism, once assembled. SMAs were coiled from a 20-mil-diameter Flexinol (nickel titanium alloy) wire using a custom winding machine, clamped in place, and annealed at 550°C for 25 min to reset their neutral configuration.

The jumping platform consisted of two conductive pads connected to four AA batteries (6 V) mounted on an acrylic support. X8 Gel-Pak was placed between the conductive pads and used as the contact surface for the striking tail.

Motion capture trajectory

The motion capture trajectory was recorded on an eight-camera near-IR Vicon T040 system. The jumping robot was equipped with five retroreflective markers. The trajectory was captured at 500 Hz.

Statistical analysis

Simulation trials

We performed a surrogate-based optimization of the jumping mechanism geometry and spring stiffness parameters. For each (spring stiffness and pulling tendon force) combination, we ran 500 solver iterations with $N \geq 6$ distinct initial parameter seeds to ensure broader coverage of the design space.

Physical prototypes

We fabricated three main prototypes of the stand-alone jumping mechanism: an unoptimized initial prototype (for early validation and high-speed video capture), a motion-capture prototype (with reflective markers) for trajectory tracking, and a dual-SMA prototype achieving the maximum jump distance. Three recorded jumps were performed with the final dual-SMA prototype, each landing around 135 ± 5 cm; we report the best jump (1.4 m) in the main paper. We attribute the small performance differences to variation in manual assembly.

Quadrupedal robot integration

We attached our jumping mechanism to the HAMR and conducted four jump trials to verify consistent performance. Each trial included a bounding maneuver to raise the robot upright, an SMA-driven jump, and a landing.

Because each jump test (whether stand-alone prototype or integrated) is effectively a single-shot high-power event, the total number of completed jumps was limited by both robot build time and SMA longevity. As a result, we do not provide statistical metrics (e.g., means and SDs over large *n*) but rather confirm that each design performs repeatably across multiple (three or four) runs.

Supplementary Materials

The PDF file includes:

Supplementary Text
Tables S1 to S5
Figs. S1 to S3
References (*59*–*68*)

Other Supplementary Material for this manuscript includes the following:

Movies S1 to S9
Data file S1

REFERENCES AND NOTES

1. Y. Chen, N. Doshi, B. Goldberg, H. Wang, R. J. Wood, Controllable water surface to underwater transition through electrowetting in a hybrid terrestrial-aquatic microrobot. *Nat. Commun.* **9**, 2495 (2018).
2. P.-L. Lechère, P. E. Schiebel, M. C. Yuen, J. Shum, R. J. Wood, Passive compliant foot design for improved micororobotic mobility on rough terrains, in *2022 IEEE/RSJ International Conference on Intelligent Robots and Systems (IROS)* (IEEE, 2022), pp. 2526–2533.
3. S. N. Patek, B. N. Nowroozi, J. E. Baio, R. L. Caldwell, A. P. Summers, Linkage mechanics and power amplification of the mantis shrimp's strike. *J. Exp. Biol.* **210**, 3677–3688 (2007).
4. E. Steinhardt, N.-S. P. Hyun, J.-S. Koh, G. Freeburn, M. H. Rosen, F. Z. Temel, S. N. Patek, R. J. Wood, A physical model of mantis shrimp for exploring the dynamics of ultrafast systems. *Proc. Natl. Acad. Sci. U.S.A.* **118**, e2026833118 (2021).
5. E. Christian, The jump of the springtails. *Naturwissenschaften* **65**, 495–496 (1978).
6. S. Sudo, M. Shiono, T. Kainuma, A. Shirai, T. Hayase, Observations on the springtail leaping organ and jumping mechanism worked by a spring. *J. Aero Aqua Bio-mechanisms* **3**, 92–96 (2013).
7. S. N. Patek, J. E. Baio, B. L. Fisher, A. V. Suarez, Multifunctionality and mechanical origins: Ballistic jaw propulsion in trap-jaw ants. *Proc. Natl. Acad. Sci. U.S.A.* **103**, 12787–12792 (2006).
8. B. R. Krasnov, S. A. Burdelov, I. S. Khokhlova, N. V. Burdelova, Sexual size dimorphism, morphological traits and jump performance in seven species of desert fleas (Siphonaptera). *J. Zool.* **261**, 181–189 (2003).
9. G. P. Sutton, M. Burrows, Biomechanics of jumping in the flea. *J. Exp. Biol.* **214**, 836–847 (2011).
10. M. E. G. Evans, The jump of the click beetle (Coleoptera, Elateridae)—a preliminary study. *J. Zool.* **167**, 319–336 (1972).
11. M. E. G. Evans, The jump of the click beetle (Coleoptera: Elateridae)—energetics and mechanics. *J. Zool.* **169**, 181–194 (1973).
12. G. Ribak, D. Weihs, Jumping without using legs: The jump of the click-beetles (Elateridae) is morphologically constrained. *PLOS ONE* **6**, e20871 (2011).
13. M. Burrows, Jumping mechanisms in jumping plant lice (Hemiptera, Sternorrhyncha, Psyllidae). *J. Exp. Biol.* **215**, 3612–3621 (2012).
14. M. Ilton, M. Saad Bhamla, X. Ma, S. M. Cox, L. L. Fitchett, Y. Kim, J.-S. Koh, D. Krishnamurthy, C.-Y. Kuo, F. Zeynep Temel, A. J. Crosby, M. Prakash, G. P. Sutton, R. J. Wood, E. Azizi, S. Bergbreiter, S. N. Patek, The principles of cascading power limits in small, fast biological and engineered systems. *Science* **360**, eaao1082 (2018).
15. S. J. Longo, S. M. Cox, E. Azizi, M. Ilton, J. P. Olberding, R. St Pierre, S. N. Patek, Beyond power amplification: Latch-mediated spring actuation is an emerging framework for the study of diverse elastic systems. *J. Exp. Biol.* **222**, jeb197889 (2019).
16. G. P. Sutton, E. Mendoza, E. Azizi, S. J. Longo, J. P. Olberding, M. Ilton, S. N. Patek, Why do large animals never actuate their jumps with latch-mediated springs? because they can jump higher without them. *Integr. Comp. Biol.* **59**, 1609–1618 (2019).
17. M. Kaspari, M. D. Weiser, The size–grain hypothesis and interspecific scaling in ants. *Funct. Ecol.* **13**, 530–538 (1999).
18. R. Kurniawan, T. Fukudome, H. Qiu, M. Takamiya, Y. Kawahara, J. Yang, R. Niiyama, An untethered 216-mg insect-sized jumping robot with wireless power transmission, in *2020 IEEE/RSJ International Conference on Intelligent Robots and Systems (IROS)* (IEEE, 2020), pp. 7881–7886.
19. J.-S. Koh, S.-P. Jung, M. Noh, S.-W. Kim, K.-J. Cho, Flea inspired catapult mechanism with active energy storage and release for small scale jumping robot, in *2013 IEEE International Conference on Robotics and Automation* (IEEE, 2013), pp. 26–31.
20. J.-S. Koh, E. Yang, G.-P. Jung, S.-P. Jung, J. H. Son, S.-I. Lee, P. G. Jablonski, R. J. Wood, H.-Y. Kim, K.-J. Cho, Jumping on water: Surface tension–dominated jumping of water striders and robotic insects. *Science* **349**, 517–521 (2015).
21. V. M. Ortega-Jimenez, E. J. Challita, B. Kim, H. Ko, M. Gwon, J.-S. Koh, M. Saad Bhamla, Directional takeoff, aerial righting, and adhesion landing of semiaquatic springtails. *Proc. Natl. Acad. Sci. U.S.A.* **119**, e2211283119 (2022).
22. Y. Wang, Q. Wang, M. Liu, Y. Qin, L. Cheng, O. Bolmin, M. Alleyne, A. Wissa, R. H. Baughman, D. Vella, S. Tawfick, Insect-scale jumping robots enabled by a dynamic buckling cascade. *Proc. Natl. Acad. Sci. U.S.A.* **120**, e2210651120 (2023).
23. J. P. Whitney, P. S. Sreetharan, K. Y. Ma, R. J. Wood, Pop-up book MEMS. *J. Micromech. Microeng.* **21**, 115021 (2011).

24. G.-P. Jung, C. S. Casarez, J. Lee, S.-M. Baek, S.-J. Yim, S.-H. Chae, R. S. Fearing, K.-J. Cho, Jumproach: A trajectory-adjustable integrated jumping–crawling robot. *IEEE/ASME Trans. Mechatron.* **24**, 947–958 (2019).
25. Y. Chen, H. Zhao, J. Mao, P. Chirarattananon, E. Farrell Helbling, N. P. Hyun, D. R. Clarke, R. J. Wood, Controlled flight of a microrobot powered by soft artificial muscles. *Nature* **575**, 324–329 (2019).
26. M. Karpelson, G.-Y. Wei, R. J. Wood, Driving high voltage piezoelectric actuators in microrobotic applications. *Sens. Actuators A Phys.* **176**, 78–89 (2012).
27. B. Kim, M. G. Lee, Y. P. Lee, Y.-I. Kim, G.-H. Lee, An earthworm-like micro robot using shape memory alloy actuator. *Sens. Actuators A Phys.* **125**, 429–437 (2006).
28. Z. Zhakypov, C. H. Belke, J. Paik, Tribot: A deployable, selfrighting and multi-locomotive origami robot, in *2017 IEEE/RSJ International Conference on Intelligent Robots and Systems (IROS)* (IEEE, 2017), pp. 5580–5586.
29. J. Zhao, W. Yan, N. Xi, M. W. Mutka, L. Xiao, A miniature 25 grams running and jumping robot, in *2014 IEEE International Conference on Robotics and Automation (ICRA)* (IEEE, 2014), pp. 5115–5120.
30. J. M. Morrey, B. Lambrecht, A. D. Horchler, R. E. Ritzmann, R. D. Quinn, Highly mobile and robust small quadruped robots, in *Proceedings 2003 IEEE/RSJ International Conference on Intelligent Robots and Systems (IROS 2003)* (IEEE, 2003), vol. 1, pp. 82–87.
31. D. Kim, M. Gwon, B. Kim, V. M. Ortega-Jimenez, S. Han, D. Kang, M. S. Bhamla, J.-S. Koh, Design of a biologically inspired water-walking robot powered by artificial muscle. *Micromachines* **13**, 627 (2022).
32. A. G. Dharmawan, H. H. Hariri, S. Foong, G. S. Soh, K. L. Wood, Steerable miniature legged robot driven by a single piezoelectric bending unimorph actuator, in *2017 IEEE International Conference on Robotics and Automation (ICRA)* (IEEE, 2017), pp. 6008–6013.
33. E. W. Schaler, L. Jiang, C. Lee, R. S. Fearing, Bidirectional, thin-film repulsive-/attractive-force electrostatic actuators for a crawling milli-robot, in *2018 International Conference on Manipulation, Automation and Robotics at Small Scales (MARSS)* (IEEE, 2018), pp. 1–8.
34. A. T. Baisch, R. J. Wood, Pop-up assembly of a quadrupedal ambulatory microrobot, in *2013 IEEE/RSJ International Conference on Intelligent Robots and Systems* (IEEE, 2013), pp. 1518–1524.
35. A. T. Baisch, O. Ozcan, B. Goldberg, D. Ithier, R. J. Wood, High speed locomotion for a quadrupedal microrobot. *Int. J. Robot. Res.* **33**, 1063–1082 (2014).
36. S. D. de Rivaz, B. Goldberg, N. Doshi, K. Jayaram, J. Zhou, R. J. Wood, Inverted and vertical climbing of a quadrupedal microrobot using electroadhesion. *Sci. Robot.* **3**, eaau3038 (2018).
37. S. C. Wells, N.-S. P. Hyun, E. Steinhardt, T. H. Nguyen, R. J. Wood, Design optimization of an ultrafast-striking mantis shrimp microrobot, in *2022 IEEE/RSJ International Conference on Intelligent Robots and Systems (IROS)* (IEEE, 2022), pp. 4236–4242.
38. F. G. L. Oliveira, A. A. Smith, A morphofunctional study of the jumping apparatus in globular springtails. *Arthropod Struct. Dev.* **79**, 101333 (2024).
39. B. Rillich, F. G. L. Oliveira, On latches in biological systems: A comparative morphological and functional study of the retinaculum and the dens lock in collembola. *Front. Zool.* **20**, 16 (2023).
40. J. Brackenbury, H. Hunt, Jumping in springtails: Mechanism and dynamics. *J. Zool.* **229**, 217–236 (1993).
41. C. Schneider, Morphological review of the order Neelipleona (Collembola) through the redescription of the type species of Acanthoneelidus, Neelides and Neelus. *Zootaxa* **4308**, 1–94 (2017).
42. P. Sardain, G. Bessonnet, Forces acting on a biped robot. Center of pressure-zero moment point. *IEEE Trans. Syst. Man Cybern. A Systems Hum.* **34**, 630–637 (2004).
43. A. Goswami, Postural stability of biped robots and the foot-rotation indicator (FRI) point. *Int. J. Robot. Res.* **18**, 523–533 (1999).
44. B. Goldberg, N. Doshi, K. Jayaram, R. J. Wood, Gait studies for a quadrupedal microrobot reveal contrasting running templates in two frequency regimes. *Bioinspir. Biomim.* **12**, 046005 (2017).
45. N. Doshi, K. Jayaram, B.Goldberg, Z. Manchester, R. J. Wood, S. Kuindersma, Contact-implicit optimization of locomotion trajectories for a quadrupedal microrobot, in *Robotics: Science and Systems XIV*, H. Kress-Gazit, S. Srinivasa, T. Howard, N. Atanasov, Eds. (RSS Foundation, 2018).
46. N. Doshi, B. Goldberg, R. Sahai, N. Jafferis, D. Aukes, R. J. Wood, J. A. Paulson, Model driven design for flexure-based microrobots, in *2015 IEEE/RSJ International Conference on Intelligent Robots and Systems (IROS)* (IEEE, 2015), pp. 4119–4126.
47. B. Goldberg, R. Zufferey, N. Doshi, E. F. Helbling, G. Whittredge, M. Kovac, R. J. Wood, Power and control autonomy for highspeed locomotion with an insect-scale legged robot. *IEEE Robot. Autom. Lett.* **3**, 987–993 (2018).
48. B. I. Goldberg, "Gait studies for a power and control autonomous legged microrobot," thesis, Harvard University (2017).
49. Z. Zhakypov, K. Mori, K. Hosoda, J. Paik, Designing minimal and scalable insect-inspired multi-locomotion millirobots. *Nature* **571**, 381–386 (2019).
50. H. C. Bennet-Clark, The energetics of the jump of the locust *Schistocerca gregaria*. *J. Exp. Biol.* **63**, 53–83 (1975).
51. M. Kovac, M. Fuchs, A. Guignard, J.-C. Zufferey, D. Floreano, A miniature 7g jumping robot, in *2008 IEEE International Conference on Robotics and Automation* (IEEE, 2008), pp. 373–378.
52. F. G. de Lima Oliveira, On springtails (Hexapoda: Collembola): A morphofunctional study of the jumping apparatus. *Front. Zool.* **19**, 21 (2022).
53. Ant Lab, Springtail jumps off water and in super slow motion! 23 March 2021; available online at https://youtube.com/watch?v=MXeSnWY6DNc.
54. E. W. Hawkes, C. Xiao, R.-A. Peloquin, C. Keeley, M. R. Begley, M. T. Pope, G. Niemeyer, Engineered jumpers overcome biological limits via work multiplication. *Nature* **604**, 657–661 (2022).
55. S. Divi, C. Reynaga, E. Azizi, S. Bergbreiter, Adapting small jumping robots to compliant environments. *J. R. Soc. Interface* **20**, 20220778 (2023).
56. F. Ramirez Serrano, E. Steinhardt, R. J. Wood, Considerations for the design and rapid manufacturing of pop-up MEMS devices. *Adv. Mater. Tech.* **9**, 2301940 (2024).
57. I. Kirk, Dunyeats hill, broadstone. Miranda 28-70zoom and 65mm of extension tubes on NexF3, 16 February 2013; https://commons.wikimedia.org/wiki/File:Springtail_%288478535939%29.jpg.
58. British Museum (Natural History), Guide to the Exhibited Series of Insects (William Clowes and Sons, 1908); available at https://biodiversitylibrary.org/bibliography/53632.
59. M. Li, X. Wang, B. Dong, M. Sitti, In-air fast response and high speed jumping and rolling of a light-driven hydrogel actuator. *Nat. Commun.* **11**, 3988 (2020).
60. C. Hong Hong, Z. Ren, C. Wang, M. Li, Y. Wu, D. Tang, W. Hu, M. Sitti, Magnetically actuated gearbox for the wireless control of millimeter-scale robots. *Sci. Robot.* **7**, eabo4401 (2022).
61. Y. Sugiyama, S. Hirai, Crawling and jumping by a deformable robot. *Int. J. Robot. Res.* **25**, 603–620 (2006).
62. C. A. Aubin, R. H. Heisser, O. Peretz, J. Timko, J. Lo, E. Farrell Helbling, S. Sobhani, A. D. Gat, R. F. Shepherd, Powerful, soft combustion actuators for insect-scale robots. *Science* **381**, 1212–1217 (2023).
63. M. Kovac, M. Schlegel, J.-C. Zufferey, D. Floreano, A miniature jumping robot with self-recovery capabilities, in *2009 IEEE/RSJ International Conference on Intelligent Robots and Systems* (IEEE, 2009), pp. 583–588.
64. Z. Yu, Y. Zeng, C. Guo, Mechanical design and performance analysis of a weevil-inspired jumping mechanism. *Machines* **10**, 161 (2022).
65. G.-P. Jung, C. S. Casarez, S.-P. Jung, R. S. Fearing, K.-J. Cho, An integrated jumping-crawling robot using height-adjustable jumping module, in *2016 IEEE International Conference on Robotics and Automation (ICRA)* (IEEE, 2016), pp. 4680–4685.
66. C. Zhang, W. Zou, L. Ma, Z. Wang, Biologically inspired jumping robots: A comprehensive review. *Robot. Auton. Syst.* **124**, 103362 (2020).
67. Y. Chen, H. Wang, E. F. Helbling, N. T. Jafferis, R. Zufferey, A. Ong, K. Ma, N. Gravish, P. Chirarattananon, M. Kovac, R. J. Wood, A biologically inspired, flapping-wing, hybrid aerial-aquatic microrobot. *Sci. Robot.* **2**, eaao5619 (2017).
68. R. Wood, S. Bergbreiter, S. Patek, Impulsive systems: Principles of rapid energy release and applications to unique robot behaviors, workshop at the 2022 International Conference on Robotics and Automation (ICRA) (IEEE, 2022); https://impulsivemuri.com/workshop2022.html.

Acknowledgments: We acknowledge J.-s. Koh for the idea and design of the reloading tendon. Thank you to P. Shiebel for assistance with the setup and controls of the tethered walking-jumping HAMR. We thank S. Wells for insights into the mechanism fabrication. Thank you to E. Christian for the springtail images. Last, we thank C. M. Barre for assistance with manufacturing. **Funding:** This material is based on work supported by, or in part by, the US Army Research Office under grant W911NF1510358. The views and conclusions contained in this document are those of the authors and should not be interpreted as representing the official policies, either expressed or implied, of the US Army Research Office or the US Government. The US Government is authorized to reproduce and distribute reprints for government purposes notwithstanding any copyright notation herein. **Author contributions:** Conceptualization: F.R.S. Manufacturing: F.R.S., P-L.L., and E.S. Simulation: F.R.S. and N.P.H. Writing—original draft: F.R.S. and P-L.L. Writing—review and editing: F.R.S. and P-L.L. Supervision: F.R.S. Project administration: R.J.W. **Competing interests:** The authors declare that they have no competing interests. **Data and materials availability:** The simulation code is available in the data repository Dryad with the following DOI: https://doi.org/10.5061/dryad.hqbzkh1t5.

Submitted 12 April 2024
Accepted 29 January 2025
Published 26 February 2025
10.1126/scirobotics.adp7854

Science Robotics

A springtail-inspired multimodal walking-jumping microrobot

Francisco Ramirez Serrano, Nak-seung Patrick Hyun, Emma Steinhardt, Pierre-Louis Lechère, and Robert J. Wood

Sci. Robot. **10** (99), eadp7854. DOI: 10.1126/scirobotics.adp7854

Science Robotics (ISSN 2470-9476) is published by the American Association for the Advancement of Science. 1200 New York Avenue NW, Washington, DC 20005. The title *Science Robotics* is a registered trademark of AAAS.